Supplemental Material for Stimulated Emission of Signal Photons from Dark Matter Waves

Ankur Agrawal, Akash V. Dixit, Tanay Roy, Srivatsan Chakram, Kevin He, Ravi K. Naik, David I. Schuster, Aaron Chou

A. Conceptual overview

For a cavity initialized in $|n\rangle$, the probability of finding the cavity in the Fock state $|l\rangle$ for a complex displacement α is described by the analytical expression [1]: $P_{nl}(|\alpha|^2) = \left|\langle l|\,\hat{\mathcal{D}}(\alpha)\,|n\rangle\right|^2 = (n!/l!)\alpha^{2(l-n)}e^{-|\alpha|^2} \times \mathcal{L}n^{l-n}(|\alpha|^2)$, where $\mathcal{L}n^{l-n}$ is an associated Laguerre polynomial. We use QuTip [2, 3] simulation tool to study the evolution of a cavity initialized in different Fock states under the action of a small displacement drive. As seen in Fig. S1, the probability of observing a dark matter induced signal is significantly enhanced for a cavity prepared in large $|n\rangle$ Fock state.

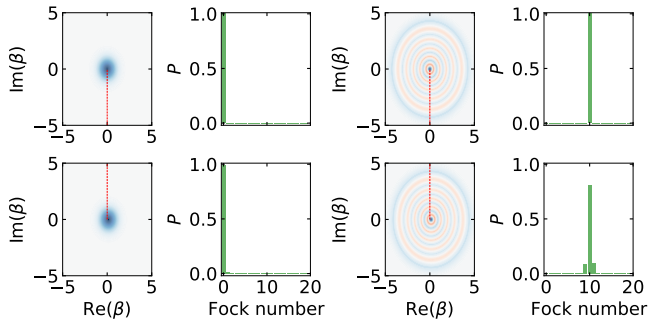

FIG. S1. **Phase-space representation of the cavity state before and after the dark matter wave push.** (Left plots) Displacing the cavity initialized in $|0\rangle$ in an arbitrary direction by a small coherent push $\beta_{\rm coh} \ll 1$ results in a small probability $P_{0,1} \propto |\mathcal{M}_{0,1}|^2$ for creating a $|1\rangle$ component by spontaneous emission of a photon from the DM wave. The direction of displacement is determined by the instantaneous phase of the DM wave which is randomized every DM coherence time, but since the initial cavity state is azimuthally symmetric, a displacement in any direction gives the same probability P_{01}. The red dashed line is shows as a guide to locate the origin w.r.t to the center of the blob. (Right plots) The cavity is initialized in a $|n\rangle = 10$ Fock state which also has an azimuthally symmetric Wigner distribution. Displacing this distribution in an arbitrary direction shifts some part of the distribution to larger radius and other parts to smaller radius. For example, the lower plots shows a displacement of $\beta_{\rm coh} = 0.1$ in the positive $X = Re(\beta)$ direction. The shift to larger radius corresponds to stimulated emission to states with larger photon number, for example $|11\rangle$ while the shift to smaller radius corresponds to stimulated absorption to states with smaller photon number, for example $|9\rangle$. As shown in the histograms, the stimulated enhancement factors $(N_{Fock}+1)$ and N_{Fock} give probabilities which satisfy $P_{10,11} = 11 \times P_{0,1}$ and $P_{10,9} = 10 \times P_{0,1}$.

B. Dark matter conversion and scan rate

The expected signal rate (R_s) from DM is proportional to the volume and the quality factor of the cavity. In DM experiments operating below 1 GHz ($h\nu \ll k_B T$), the background rate (R_b) is limited by the thermal occupation of the cavity such that the noise added by an amplifier in the readout process is sub-dominant. However, at frequencies in $5-30$ GHz range, the DM search faces major challenges as the signal-to-noise ratio (SNR) rapidly plummets down.

The expected DM signal decreases at higher frequencies due to following reasons: (1) the cavity volume diminishes as the cavity dimensions shrink to maintain the resonance condition ($V \propto \nu^{-3}$) for a TM_{0n0} type mode, (2) the quality factor of a normal metal cavity degrades due to the anomalous skin effect [4, 5]. Moreover, the noise from quantum-limited readout process increases at higher frequencies because the power scales as $h\nu\,(\frac{\nu}{Q_{\rm DM}})$, where $Q_{\rm DM}$ is the quality factor of a DM wave given by the escape velocity of DM from the galaxy. The first term in the expression represents the energy of one photon, which is determined by the standard quantum limit. This limit specifies that the minimum amount of noise added by an amplifier is equivalent to a mean photon number of $\bar{n}_{SQL} \geq 1$[6, 7, 8, 9, 10]. The signal frequency scan rate R (in Hz/s), a key merit of haloscope type experiment, is proportional to $\propto R_s^2/R_b$ as shown in Eq. (S1). Quantum-enhanced techniques to improve signal rate and reduce noise are required to improve SNR and hence accelerate the search for the extremely weak dark matter signal.

The integration time (Δt) required for a background limited dark matter search is given by the time required to achieve 1σ sensitivity determined by Poisson counting statistics: $R_s \Delta t > \sqrt{R_b \Delta t}$, where $R_s = \bar{n}_{\rm HP}/\tau$ and background rate $R_b = \bar{n}_c^b/\tau$. The signal accumulation time for each Fock state preparation is given by τ. For an optimal dark matter scanning experiment, we would want to start with a high-Q cavity ($Q_{\rm cav} > Q_{\rm DM}$) in the largest possible Fock state $|n\rangle$ such that τ (which must be smaller than the Fock state coherence time $Q_{cav}/(\nu * n)$) can be matched with the signal coherence time $Q_{\rm DM}/\nu$. Hence, the integration time at each frequency point scales as R_b/R_s^2 and, the scan rate is given by,

$$R = \Delta\nu/\Delta t = (\frac{\nu}{Q_{\rm DM}})\frac{1}{N_{\rm trials}\,\tau} \propto R_s^2/R_b, \qquad \text{(S1)}$$

such that Δt is the sum of many iterations of duration

τ and N_{trials} is the total number of iterations for each Fock state preparation. While the stimulated emission technique will generally enhance R_s by a factor $(n+1)$, the coherence time of the prepared quantum state is also reduced by a factor $(n+1)$, thus also restricting the accumulation time τ. The smaller coherence time then necessitates a faster readout rate which then generally causes the background rate R_b to also increase by a factor $(n+1)$ for backgrounds which are associated with the readout procedure or due to a residual non-zero mode occupation number in the cavity. The overall improvement in $d\nu/dt$ due to Fock enhancement is then a single factor $\eta\,(n+1)$, where η is the detection efficiency in the experiment.

Each measurement sequence consists of state preparation and validation ($2\,\mu\text{s} + 3 \times t_m = 17\,\mu\text{s}$), signal integration ($20\,\mu\text{s}$) and 30 repeated measurements ($30 \times t_m = 150\,\mu\text{s}$). There is an additional dead time in the experiment due to imperfect state preparation which constitutes $35\% \times 17\,\mu\text{s} \approx 6\,\mu\text{s}$ for $|n=4\rangle$ Fock state. The total search time at each Fock state is roughly $20,000 \times 193\,\mu\text{s} = 36.6\,\text{s}$ with a duty cycle of $\frac{20}{193} = 10\%$ (3.6 s of integration). For the present apparatus, the duty cycle could be increased to $\sim 30\%$ if longer signal integration times are chosen at the expense of greater systematics due to Fock state decoherence. Higher Q cavities would enable even larger integration times and duty cycles.

C. Experimental setup

The cavities and qubit are mounted to the base plate of a dilution fridge (Bluefors LD400) operating at 10 mK. Fig. S3 shows an image of the actual device, which is housed in two layers of μ-metal to shield from magnetic fields. Signals sent to the device are attenuated and thermalized at each temperature stage of the cryostat as shown in Fig. S2. The field probing the readout resonator is injected via the weakly coupled port (shorter dipole stub antenna). Control pulse for the qubit are inserted through the strongly coupled readout port (longer dipole stub antenna). The storage cavity is driven through a direct port which is weakly coupled to the external microwave chain. Both control lines also contain an inline copper coated XMA attenuator that is threaded to the base plate. The signal from the readout resonator reflects off a Josephson parametric amplifier before being amplified by a cryogenic HEMT amplifier at the 4 K stage. The output is mixed down to 100 MHz IF signal before being digitized. Cavity and transmon fabrication details can be found in Supplemental materials of Ref. [11, 12].

D. Fock state preparation and characterization

In several recent works, it has been demonstrated that a single transmon is capable of preparing any quantum state in the cavity and perform universal control on it. The methods developed include - resonant swap of a qubit excitation to the cavity [14], SNAP gates

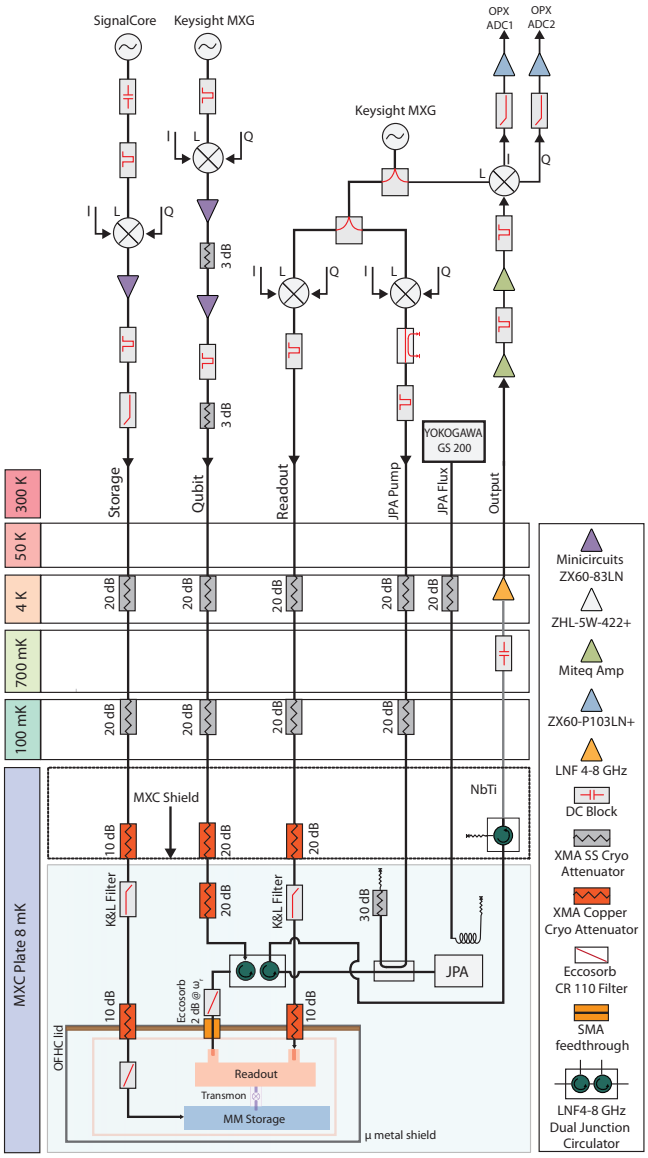

FIG. S2. **Wiring diagram inside the dilution refrigerator and the room temperature measurement setup.** Quantum Machines (QM) OPX controller was used to generate the arbitrary wave forms (DACs) and digitize the incoming readout signal (ADCs). All the tones are up-converted using IQ modulation, with local oscillator (LO) and AWG synced to an SRS F2575 RB source. Storage cavity is controlled via a direct port and qubit is controlled by injecting a drive into the strongly coupled port of the readout. Readout signal is injected into the weakly coupled port, and the signal is routed to the JPA using non reciprocal circulator elements. The amplified signal is routed to the HEMT for further amplification and the signal is then mixed down to 100 MHz IF, further amplified, and finally digitized. All the RF lines are heavily filtered with homemade eccosorb filters and attenuated to minimize stray radiation from entering the device.

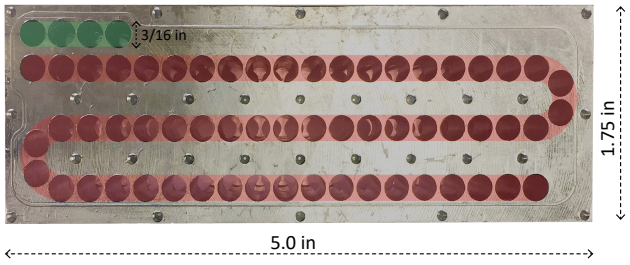

FIG. S3. **Multimode cavity**. Image of a microwave cavity fabricated using the flute method [13]. The storage and readout cavities are indicated in red and green, respectively. The cavity volumes are carved out of a monolithic Aluminum block (height = 2.25 in) by drilling offset holes from the top and the bottom surfaces using a 3/16-inch drill bit.

[15], Blockade [12], and GRadient Ascent Pulse Engineering (GRAPE) based optimal control (OCT) pulses [16, 17] and Echoed Conditional Displacement (ECD) control pulses [18] to solve the inversion problem of finding control fields to transfer a quantum system from state A to B. We use a GRAPE based method to generate a set of optimal control pulses [16, 17] to prepare non-classical states in an cavity. In the optimal control, we consider the full model of the time dependent Hamiltonian and generate the control pulses which maximizes the target state fidelity as has been previously demonstrated in nuclear magnetic resonance experiments [19] as well as superconducting circuits [17]. The main advantage of this approach is that the duration of state preparation pulses can be as short as $1/\chi$ and does not necessarily increase for higher Fock states [17, 18]. We use OCT pulses to successfully prepare cavity Fock states as shown in Fig. 1 (b).

We briefly investigated the SNAP protocol [15] to prepare Fock states but did not pursue further as it suffers from two issues limiting the maximum achievable fidelity. First, the number of constructed sequences scales as $(2n+1)$, requiring large number of gates, limiting operations which are feasible in the presence of decoherence. Second, the constructed model fails to account for the higher order Kerr non-linearity ($\mathcal{H}_{Kerr}/\hbar = K(a^\dagger)^2(a)^2$) in the Hamiltonian, which is non-negligible at higher photon occupation. This results in finite occupation probability at the other Fock states as well.

We know that a Fock state has a definite photon number but no definite phase associated with it. Therefore, a simple qubit spectroscopy reveals as much as information as a Wigner tomogram would do. However, we use both these methods to compute and confirm the presence of Fock states in the cavity. Fig. 1 (b) shows the qubit spectroscopy (top) and Wigner tomography (bottom) of the resultant Fock states. Qubit spectroscopy is performed immediately after the optimal control (OCT) pulses, a single peak in each qubit excitation probability (P_e) distribution confirms the creation of the correct $|n\rangle$ Fock state. Resultant probability distribution is fitted to a Gaussian to estimate the state preparation fidelity. Grey dashed lines correspond to the expected shift in frequency, accounted for quadratic dispersive shift. Wigner tomography [20] is performed by coherently displacing the resultant cavity state in 2D phase space to map the average parity and thus, reconstruct the cavity state density matrix.

The Wigner tomogram of a particular cavity state is quasi-probability distribution and is a function on a pair of conjugate variables. The marginal distribution obtained by integrating along one of these variables gives the probability distribution in the other variable. Wigner tomography is a useful metric to determine the non classicality of a state. The key features of non-classical states is the negativity of Wigner function. We refer readers to [21] (page 35-37) for an excellent discussion on the relation between Wigner function and the photon number parity of a cavity state, measurement procedure and how to reconstruct the density matrix of a quantum state in the cavity.

Moreover, we study the evolution of the cavity under the action of OCT pulses by tracking the cavity state as shown in Fig. S4 (b). We perform a number resolved qubit spectroscopy at different points in time to map out the occupation probability of different Fock levels, in agreement with the simulated trajectory.

E. Calibration of number resolved π ulse

In order to successfully probe the presence of Fock states in the cavity, we need a very well calibrated narrow bandwidth π-pulse - amplitude as well as frequency. We perform an amplitude Rabi experiment with a $3\,\mu$s (4σ) long Gaussian pulse such that its spectral spread is smaller than the χ-shift. After a coarse amplitude sweep, we perform a finer sweep centered at the initial guess and apply a set of 12 Gaussian pulses in succession to amplify any gate errors such as under/over rotation, frequency drift to get a better estimate of the π-pulse amplitude. For qubit transition frequency, we initialize the cavity in a particular Fock state $|n\rangle$ and perform a qubit Ramsey interferometry experiment. It consists of two $\pi/2$ pulses separated by a variable delay time. A Fast Fourier Transform (FFT) of the resultant time oscillations gives the shift in the qubit transition frequency which accounts for any higher order corrections as well. The computed transition frequencies and amplitude are used in the actual experiment to minimize the errors.

F. Device calibration

By applying a weak coherent tone at the storage cavity frequency, we induce a variable displacement α of the cavity state. We calibrate the number of photons injected into the storage cavity by varying the drive amplitude and performing qubit spectroscopy. By fitting the qubit spectrum as shown in Fig. S5 to a Poisson distribution, we extract the cavity occupation, $\bar{n} = |\alpha|^2$. Similarly, the qubit drive strength is calibrated by per-

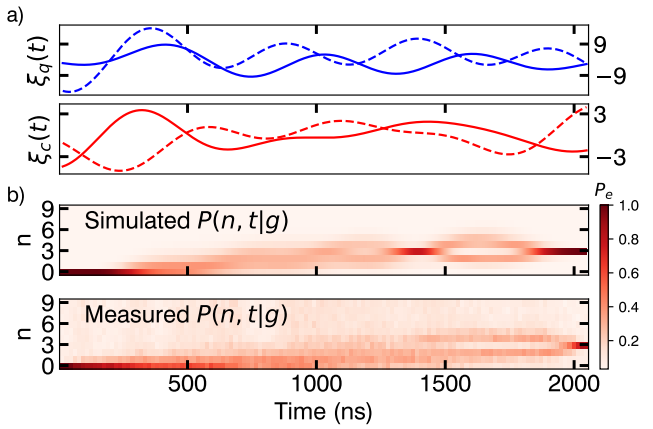

FIG. S4. **Fock state preparation in a cavity dispersively coupled to a transmon qubit**. **(a)** Optimized control drives to the qubit (top) and cavity (bottom) to transfer the qubit-cavity state from $|g, 0\rangle \rightarrow |g, 3\rangle$. The drive strengths are in units of MHz. **(b)** Simulated trajectory of the cavity state using QuTip under the control drive. Measured cavity occupation probability showing all the levels explored during the evolution before converging to the desired state $|g, 3\rangle$ at the end. The experiment involves playing a fraction of the OCT pulses and performing qubit spectroscopy with a number resolved π-pulse. Each vertical slice corresponds to the cavity occupation probability in different number states as function of the duration of pulse. Note that the simulation does not include the presence of neighboring cavity modes as well as the measurement infidelity. Control fields for the qubit and cavity are generated by a room temperature field-programmable gate array (FPGA) controller, which also provides a low-latency feedback signal to actively monitor the state of the cavity.

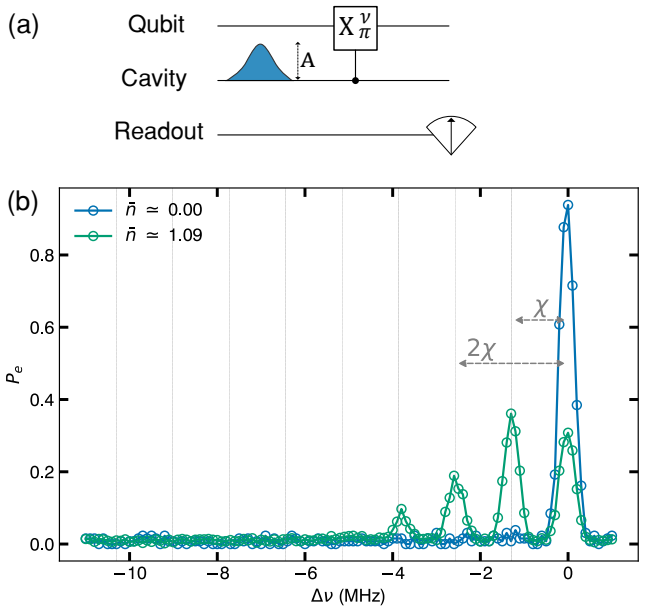

FIG. S5. **Qubit spectroscopy reveals cavity displacement** (a) Pulse sequence showing the calibration of cavity photon number by performing qubit spectroscopy. (b) The cavity is displaced using a variable weak coherent drive for a finite period of time. The resulting population of the cavity is determined by performing qubit spectroscopy with a resolved π-pulse. The cavity photon number dependent shift of the qubit transition frequency reveals the cavity population. By fitting the spectrum to a Poisson distribution we extract the weights of the cavity number states in the prepared coherent state and thus, the mean photon occupation.

forming qubit Rabi experiments with varying AWG amplitude and pulse length. The measured drive strength and the AWG amplitude mapping is used to send the correct OCT pulses to the device. See Supp. section in [11] and [13] for more details on device parameter calibrations.

G. Hidden Markov model analysis

We adopt the Hidden Markov Model (HMM) approach presented in [11] to consider all the possible errors that may occur during the measurement process and alter the state of the cavity, qubit, and readout. The cavity and qubit states are treated as hidden variables that emit readout signals. The Markov chain is modeled by the transition matrix (T) (Eq. (S3)) which describes the evolution of the joint cavity-qubit hidden state $s \in [|n'g\rangle, |n'e\rangle, |ng\rangle, |ne\rangle]$ and the emission matrix (E) (Eq. (S4)) that calculates the probability of a readout signal $R \in [\mathcal{G}, \mathcal{E}]$ given a certain hidden state. It's important to note that with a number-resolved π-pulse centered at the n-shifted peak, we can only determine whether the cavity is in the $|n\rangle$ Fock state or not ($|n' \neq n\rangle$). During this course, the first measurement collapses the cavity state to either $|n+1\rangle$ or not. If in $|n+1\rangle$, the subsequent measurements are QND and via the quantum Zeno effect, each measurement resets the clock on the decay of the $|n+1\rangle$ state.

The transition and emission matrix were first introduced in [22] and implemented in [11]. The change in qubit state probability is not affected by the cavity state. However, the repeated measurement of the cavity state with a number selective π-pulse introduces an additional channel through which the cavity loses its excitation. It is called demolition probability (p_d), which signifies the non-QNDness of the projective measurement of the cavity state with the qubit. In simple terms, a single qubit measurement is $(1 - p_D)\%$ QND. We followed the protocol described in Ref.[23] for repeated parity measurement and replaced it with number selective π-pulse. Table S1 and Fig. S9 show the measured values for different Fock states. The elements of the emission matrix represent the readout fidelities for the ground and excited states of the qubit, which are influenced by noise from the first stage JPA. More information on the experimental protocols used can be found in the supplemental material.

We used the backward algorithm (Eq. (S2)) [22, 24] to calculate the probability ($P(n_0)$) that the cavity state was in the $|n+1\rangle$ Fock state after the injection of a synthetic DM signal. The algorithm takes a set of $N+1$ mea-

sured readout signals $(R_0, R_1, ..., R_N)$ as input, where $n_0 = n + 1$ represents the target Fock state and n_0' can take on values in the range $[0, n, n + 2, ...]$.

$$P(n_0) = \sum_{s_0 \in [|n_0,g\rangle, |n_0,e\rangle]} \sum_{s_1} ... \sum_{s_N} E_{s_0,R_0} T_{s_0,s_1} E_{s_1,R_1} \cdots T_{s_{N-1},s_N} E_{s_N,R_N} \tag{S2}$$

In the reconstruction process, all possible scenarios are taken into account. For instance, a readout measurement of $\mathcal{G}$ followed by $\mathcal{E}$ could happen due to the successful detection of the cavity in the $|n+1\rangle$ state with a probability of $P_{n_0 n_0} P_{gg} F_{e\mathcal{E}}/2$. On the other hand, it could also be caused by either a qubit heating event $(P_{n_0' n_0'} P_{ge} F_{e\mathcal{E}}/2)$ or a readout error $(P_{n_0' n_0'} P_{gg} F_{g\mathcal{E}}/2)$. The data in Fig. 2(b) illustrates the results of the measurement of the readout signals and the reconstructed initial probabilities of the cavity state. The panels on the left show instances when there was no emission event, while the panels on the right depict cases where a positive emission event took place. The cavity state shifted from $|1\rangle$ to $|2\rangle$ as a result of a variable displacement drive $\mathcal{D}(\alpha)$, and the change was accurately reflected in the reconstructed probability.

The reconstructed cavity state probabilities undergo a likelihood ratio test $(\lambda = \frac{P(n_0=n+1)}{P(n_0\neq n+1)})$ to determine if the cavity state changed or not. A positive detection of a photon signal $|n\rangle \rightarrow |n+1\rangle$ is declared when the threshold $\lambda > \lambda_{\text{thresh}}$. The false positive rate is limited to less than $\frac{1}{\lambda_{\text{thresh}}+1}$ as a result of this procedure. A higher detection threshold can be achieved by increasing the number of repeated measurements, but at the cost of decreased efficiency which is linear in the number of measurements. Hence, λ_{thresh} is chosen to strike a balance between the detection efficiency and the false positive rate, keeping it below the observed physical photon background. This will be discussed further in the next section.

H. Elements of hidden Markov model

The hidden Markov model relies on independent measurements of the probabilities contained in the transition and emission matrices. The elements of these matrices depend on the parameters of the experiment and the device, including the lifetimes of the qubit and cavity, qubit spurious population, and readout fidelities.

Transmission matrix elements

The transition matrix captures the possible qubit (cavity) state changes. Qubit relaxation $|e\rangle \rightarrow |g\rangle$ occurs with a probability $P_{eg}^{\downarrow} = 1 - e^{-t_m/T_1^q}$. The probability of spontaneous heating $|g\rangle \rightarrow |e\rangle$ of the qubit towards its steady state population is given by $P_{ge}^{\uparrow} = \bar{n}_q[1-e^{-t_m/T_1^q}]$. Unlike a two-level system such as a qubit, the cavity state may change from $|n\rangle \rightarrow |n'\rangle$ via either decay $(|n\rangle \rightarrow |n-1\rangle)$ or excitation $(|n\rangle \rightarrow |n+1\rangle)$ with probabilities $P_{n,n-1} = 1-e^{-t_m/T_1^n}$ or $P_{n,n+1} = \bar{n}_c[1-e^{-t_m/T_1^n}]$ respectively. The lifetime of the Fock state is modified due to the enhanced decay [14] $(T_1^n = T_1^s/n)$ as compared to the bare lifetime of a coherent state (see Supp Fig. S8). Yet another possible source of change in the cavity state is the repeated qubit measurement itself. In most cases, we assume the interaction between the qubit and cavity to be QND, i.e., the measurement of cavity state by qubit does not perturb the state. However, we measured the QNDness of repeated qubit measurement for $|n\rangle = 1$ Fock state to be 97.4% which corresponds to a demolition probability p_d of 2.6% per measurement (see Fig. S9). Hence, we add this term in the transition matrix. All these probabilities are computed using independently measured qubit, cavity and readout parameters described below.

$$T = \begin{array}{c} \begin{matrix} |n'g\rangle & |n'e\rangle & |ng\rangle & |ne\rangle \end{matrix} \\ \begin{bmatrix} P_{n'n'}P_{gg} & P_{n'n'}P_{ge} & P_{n'n}P_{ge} & P_{n'n}P_{gg} \\ P_{n'n'}P_{eg} & P_{n'n'}P_{ee} & P_{n'n}P_{eg} & P_{n'n}P_{ee} \\ P_{nn'}P_{gg} & P_{nn'}P_{ge} & P_{nn}P_{ge} & P_{nn}P_{gg} \\ P_{nn'}P_{eg} & P_{nn'}P_{ee} & P_{nn}P_{ee} & P_{nn}P_{eg} \end{bmatrix} \end{array} \begin{matrix} |n'g\rangle \\ |n'e\rangle \\ |ng\rangle \\ |ne\rangle \end{matrix} \tag{S3}$$

The lifetime of the qubit is determined by applying a π pulse and waiting for a variable time before measuring the population as shown in Fig. S6. We map out the qubit population as a function of the delay time, fit it with an exponential characterizing the Poissonian nature of the decay process, and obtain $T_1^q = 115 \pm 10\,\mu$s.

The dephasing time of the qubit is measured by a Ramsey interferometry experiment with a $\pi/2$ pulse, variable delay, and a final $\pi/2$ with its phase advanced by $\omega_r t$ where ω_r is the Ramsey frequency. The phase advancement is implemented in the software. During the variable delay period, a series of π pulses are applied to perform spin echos and reduce sensitivity to low frequency noise. We observe a dephasing time of $T_2^q = 160 \pm 10\,\mu$s which extends to $T_2^e = 236 \pm 6\,\mu$s with a single echo sequence.

The storage cavity lifetime is calibrated by performing a cavity T_1 experiment. We use the OCT pulse to prepare the cavity in a $|n\rangle = 1$ Fock state, wait for a variable delay time and probe the cavity state at the end by Rabi driving the qubit with a resolved π-pulse. The resultant cavity population is fitted to an exponential to obtain $T_1^s = 1.36 \pm 0.02$ ms as shown in Fig. S7. To measure the cavity dephasing time, the cavity is initialized in a superposition state $(a\,|0\rangle + b\,|1\rangle)$ by applying a weak coherent drive (α) such that approximately only the first two photon states $|n\rangle$ are populated. The contrast in the signal will be determined by the relative amplitude $(\frac{a^2}{a^2+b^2})$ without any loss of information. After a variable delay time, an identical displacement drive with its phase advanced by $\omega_r\, t$ is applied before probing the $|n\rangle = 0$ with a resolved π-pulse on the qubit. The oscillations are fitted to obtain a dephasing time of $T_2^s = 2.39 \pm 0.02$ ms.

The qubit spurious population is determined by measuring the relative populations of its ground and excited states [25]. This is done by utilizing the f-level of the transmon. Two Rabi experiments are conducted swapping population between the $|e\rangle$ and $|f\rangle$ levels. First, we

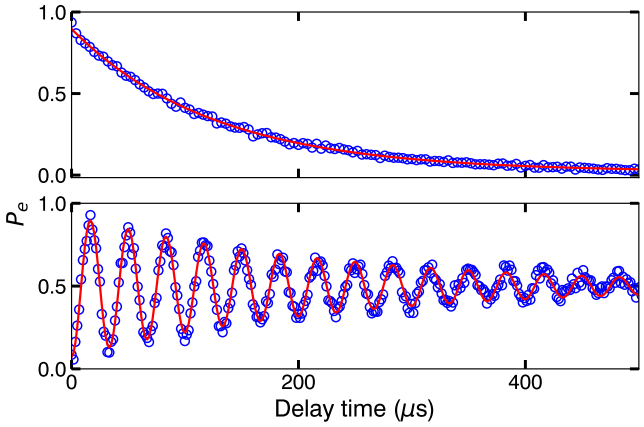

FIG. S6. **Qubit lifetime and dephasing time measurement.** (Top) T_1 measurement by sending a π-pulse to excite the transmon to $|e\rangle$ state and monitor its decay as a function of variable delay time. By fitting an exponential function to the qubit excitation probability P_e, we extract the $T_1^q = 115 \pm 10\,\mu$s. (Bottom) T_2 measurement with a Ramsey experiment. The sequence consists of two $\pi/2$-pulse separated by a variable delay time. The envelope of the measured oscillations informs the $T_2^e = 236 \pm 6\,\mu$s and its frequency provides us the detuning between the drive and the transmon resonance frequency. In this case, we intentionally introduced a 60 kHz synthetic detuning.

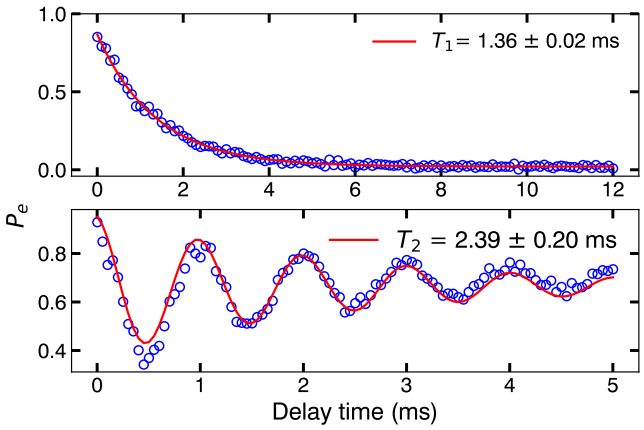

FIG. S7. **Storage cavity lifetime and dephasing time from T_1 and Ramsey measurements.** The long lived storage cavity mode is ideal for holding a signal photon induced by the dark matter while a series of repeated photon counting measurements is performed.

apply a π_{ge} pulse to invert the qubit population followed by the $|e\rangle - |f\rangle$ Rabi experiment. Second, no π_{ge} pulse is applied before the ef Rabi oscillation. The ratio of the amplitudes of the oscillations gives us the ratio of the populations of the excited and ground state. Assuming that $P(g) + P(e) = 1$ and measuring $\frac{P(e)}{P(g)} = 0.02$, corresponds to an effective qubit temperature of 54 mK.

In a dispersive interaction, we assume that the measurement of cavity state via a parity or number resolved π-pulse does not perturbed the state i.e. it is a quantum non-demolition (QND) measurement or in other words, does not induce additional relaxation in the cavity mode. However, a recent study has shown that parity measurements, while highly QND, can induce a small amount of additional relaxation [23]. Hence, in order to estimate the same, but, in the context of number resolved qubit measurement, we follow the method described in [23], where we perform a cavity T_1 experiment interleaved with varying number of repeated number resolved qubit measurements during the delay time. In that experiment, the total relaxation rate was modeled as a combination of the bare storage lifetime τ_s and a demolition probability p_d associated with each qubit measurement. In Fig. S9, we show the extracted total decay time ($\tau_{\rm tot}$) and demolition probability $p_d = 2 \pm 0.02\%$ when the cavity is prepared in $|n\rangle = 1$ Fock state. In other words, a single number resolved qubit measurement is 98% QND. Unfortunately, for $|n\rangle = 2$, $p_d = 4 \pm 0.04\%$ gets worse, which is not a good sign but probably explains why the detection efficiency in Fig. 3 falls off at higher Fock states. This acts like an additional source of loss to the cavity mode but only when the resolved π-pulse is on resonance with the shifted qubit frequency.

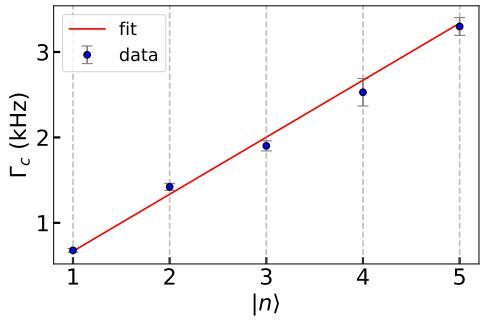

FIG. S8. **Decay rate of Fock states.** Measured lifetime of the different Fock states prepared in the cavity using GRAPE pulses. The decay rate is inversely proportional to the lifetime ($\Gamma = 1/T_1$). The curve shows enhancement in the decay rate as a function of the Fock state $|n\rangle$. The linear fit to the data fits well as predicted by [26], where $T_1^n = T_1/n$.

$\|n\rangle$	$\tau_s(\mu s)$	p_d	σ_{p_d}
$\|1\rangle$	1360	0.026	0.002
$\|2\rangle$	660	0.040	0.004
$\|3\rangle$	527	0.10	0.05
$\|4\rangle$	319	0.074	0.012

TABLE S1. **Demolition probability**. Measured lifetime of the different Fock states and their fitted demolition probability with error bars. p_d can be approximated with a linear dependence on n.

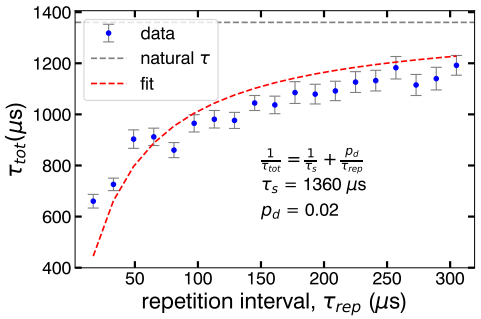

FIG. S9. **QNDness of storage cavity measurement.** Storage cavity T_1 measurements were performed with repeated number resolved qubit measurements interleaved during the delay time with a variable repetition interval time $\tau_{\rm rep}$. The extracted total decay time was fit to a model $1/\tau_{\rm tot} = 1/\tau_s + p_d/\tau_{\rm rep}$. From the fit (red line), we infer a demolition probability per readout of $p_d = 2.6\%$ corresponding to a QNDness of 97.4%, which is a bit lower than reported for a parity protocol [23]. The natural decay time of the storage $\tau_s = 1360\,\mu$s is indicated by a dashed grey line.

Emission matrix elements

In order to characterize the emission matrix it is necessary to measure the readout infidelity of a particular transmon state. We consider only two possible transmon states ($|g\rangle, |e\rangle$) in this case as the number resolved π-pulses have very narrow spectral width ($\sigma_\nu \ll \alpha_q$). Each state is prepared 20,000 times and the resultant quadrature values are digitized to assign a voltage in the $(I-Q)$ space. The phase of the readout pulse is precalibrated to align the signal along the I axis. The histogram corresponding to each state is fitted with a sum of two Gaussian functions to estimate the overlap region and calculate the readout fidelity, $\mathcal{F} = 97\%$ (Fig. S10). A discriminator value (red dashed line) is used to assign each readout signal either $\mathcal{G}$ or $\mathcal{E}$ in real-time.

$$E = \frac{1}{2}\begin{array}{c} \begin{matrix} \mathcal{G} & \mathcal{E} \end{matrix} \\ \begin{bmatrix} F_{g\mathcal{G}} & F_{g\mathcal{E}} \\ F_{e\mathcal{G}} & F_{e\mathcal{E}} \\ F_{g\mathcal{G}} & F_{g\mathcal{E}} \\ F_{e\mathcal{G}} & F_{e\mathcal{E}} \end{bmatrix} \end{array} \begin{matrix} |n'g\rangle \\ |n'e\rangle \\ |ng\rangle \\ |ne\rangle \end{matrix} \tag{S4}$$

Readout errors are due to voltage excursions from amplifier noise or spurious qubit transitions. The emission matrix should only contain readout errors that occur due to voltage fluctuations. Errors due to qubit transitions during the readout window are accounted for in the transition matrix. To disentangle the two contributions, we subtract the readout errors caused by the spontaneous heating and decay of the qubit to obtain $F_{g\mathcal{G}} = 97.5 \pm 1\%$ and $F_{e\mathcal{E}} = 96.8 \pm 1\%$.

I. Detector characterization

To characterize the detector, the cavity population is varied by applying a weak drive and the cavity photon number is counted using the technique described in the main text. In order to extract the efficiency (η) and false positive probability (δ) of the detector, the relationship between injected photon population ($\bar{n}_{\rm inj}$) and measured photon population ($\bar{n}_{\rm meas}$) is fit to $\bar{n}_{\rm meas} = \eta \times \bar{n}_{\rm inj} + \delta$.

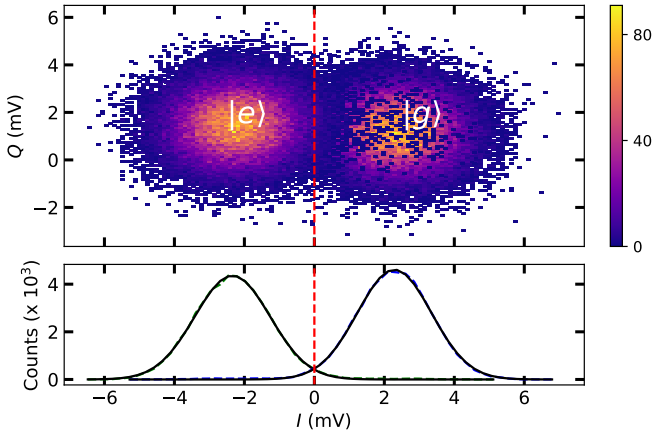

FIG. S10. **QND readout of the transmon state.** (Top) shows the two quadrature values of the down-converted readout signal for qubit prepared in $|g\rangle$ and $|e\rangle$ state. Each state preparation contains 20,000 single shot points. (Bottom) By fitting a sum of two Gaussian we can estimate the overlap region and assign a single-shot readout fidelity as $\mathcal{F} = 97\%$. The red dashed line shows an optimal value of the threshold for tagging a qubit state based on a single shot readout.

Device Parameter	Value
Qubit frequency	$\omega_q = 2\pi \times 4.961\,$GHz
Qubit anharmonicity	$\alpha_q = -2\pi \times 143.2\,$MHz
Qubit decay time	$T_1^q = 115 \pm 10\,\mu$s
Qubit dephasing time	$T_2^q = 160 \pm 10\,\mu$s
Qubit echo time	$T_2^e = 236 \pm 6\,\mu$s
Qubit residual occupation	$\bar{n}_q = 2 \pm 1 \times 10^{-2}$
Storage frequency	$\omega_s = 2\pi \times 5.965\,$GHz
Storage decay time	$T_1^s = 1360 \pm 23\,\mu$s
Storage dephasing time	$T_2^s = 2390 \pm 286\,\mu$s
Storage-Qubit Stark shift	$\chi = -2\pi \times 1.285\,$MHz
Storage residual occupation	$\bar{n}_c = 6.3 \pm 3 \times 10^{-3}$
Readout frequency	$\omega_r = 2\pi \times 7.790\,$GHz
Readout $\|e\rangle$ shift	$2\chi_r^e = -2\pi \times 1.53\,$MHz
Readout fidelity ($\|g\rangle$)	$F_{g\mathcal{G}} = 97.5 \pm 1\%$
Readout fidelity ($\|e\rangle$)	$F_{e\mathcal{E}} = 96.8 \pm 1\%$

TABLE S2. **Device parameters**. Measured qubit, storage, and readout cavity parameters. These independently measured values are necessary to determine for the transition and emission matrices. This enables the hidden Markov model to capture the behavior of the system during the measurement sequence.

Detector efficiency

The detector efficiency and false positive probability is determined at varying thresholds for detection λ_{thresh}. As the detection threshold is increased, more repeated number resolved qubit measurements are required to determine the presence of a photon. This suppresses false positives due to qubit errors but also leads to a decrease in the detector efficiency as events with low likelihood ratio are now rejected. Also, the maximum achievable likelihood ratio decreases with the Fock state prepared in the cavity. Hence, we decided to keep the false positive probability same for comparing different Fock states at the expense of detection efficiency. In Fig. 3, we observe a decrease in detection efficiency for higher Fock states which can be explained by the higher decay and demolition probability to achieve the fixed likelihood ratio threshold used for the comparison. For example, consider the $|n=5\rangle$ Fock state. During the course of 30 repeated measurements, it is 1.6 times more likely to decay than the $|n=1\rangle$ Fock state. In addition, the higher demolition probability 0.074 for $|n=4\rangle$ makes it more difficult to achieve high likelihood ratio since this photon state only persists for the first 14 quasi-QND measurements. We performed a single photon counting experiment [11] to determine the occupation number of the background photons in the cavity (Fig. S11) and chose the threshold such that $\frac{1}{\lambda_{\text{thresh}}+1} < \bar{n}_b^c \Rightarrow \lambda_{\text{thresh}} = 10^3$. This measured background translates into a metrological gain of 11.0 dB below the SQL.

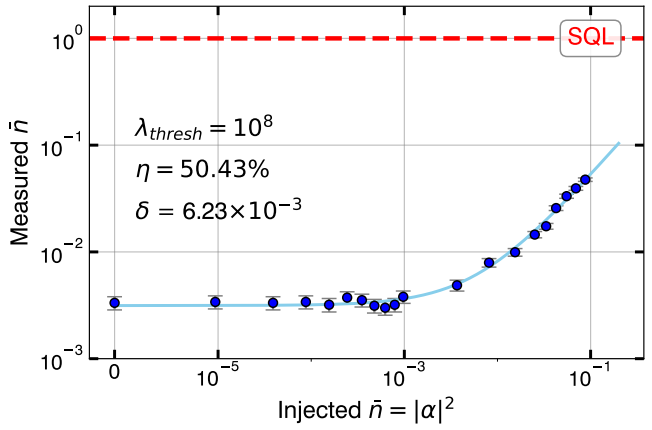

FIG. S11. **Photon counting to measure the cavity background.** Repeated parity measurement technique followed from [11] to measure the real photon occupation in the cavity $\bar{n}_b^c = 6.23 \cdot 10^{-3}$ with detector based errors less than 10^{-8}.

A. *Cavity backgrounds*

The number of events which cross λ_{thresh} for cavity prepared in different Fock states are not same, and are subtracted from the $\alpha \neq 0$ events to demonstrate the enhancement effect. The number of such events are listed in the table below and are similar to the false positive probability from the fits in Fig. 3. The number of counts are corrected for the detection efficiency to reflect the actual counts. There is no reason to expect the number of counts would increase with n and we include them in the systematic uncertainties while conducting a dark photon search. In an independent dataset, we observe a similar number of counts as reported in Fig. 4.

$\|n\rangle$	N_{trials}	N_{bkgd}	%
$\|0\rangle$	114915	23	0.020
$\|1\rangle$	111601	315	0.282
$\|2\rangle$	113364	60	0.053
$\|4\rangle$	108626	827	0.761

TABLE S3. **Background counts**. Number of background counts N_{bkgd} reported for cavity initialized in different Fock states out of N_{trials}.

J. Converting background counts to dark photon exclusion

As described in the main text, for a coherent source we expect the signal rate to be proportional to the term a_0. We will derive the expression and compute the kinetic mixing angle which corresponds to a_0. See Supplementary Section in Ref. [11] for discussion about dark matter induced signal.

Kinetic mixing angle exclusion

For a dark matter candidate on resonance with the cavity frequency ($m_{\text{DM}}c^2 = \hbar\omega_c$), the rate of photons deposited in the cavity prepared in a Fock state $|n\rangle$ by the coherent build up of electric field in time τ ($\tau < T_1^s, Q_{\text{DM}}/\nu$) is given by:

$$\frac{dN_{\text{HP}}}{dt} = \frac{U/\omega_s}{\tau} = \frac{1}{2}\frac{E^2 V}{\omega_s}\frac{1}{\tau} = \frac{1}{2}J_{\text{DM}}^2(n+1)\tau^2\frac{GV}{\omega_s}\frac{1}{\tau} \tag{S5}$$

The stimulated emission factor appears via the enhancement of magnitude of the electric field generated inside the cavity. The volume of the cavity is $34.5 \times 0.5 \times 2.5\,\text{cm}^3 = 43.13\,\text{cm}^3$. $\mathcal{G}$ encompasses the total geometric factor of the particular cavity used in the experiment. This includes a factor of 1/3 due to the dark matter field polarization being randomly oriented every coherence time. For the lowest order mode of the rectangular cavity coupled to the qubit with $\mathbf{E} = (\frac{\pi x}{l})(\frac{\pi y}{w})\mathbf{z}$ the geometric form factor is given by:

$$G = \frac{1}{3}\frac{\left|\int dV E_z\right|^2}{V\int dV\,|E_z|^2} = \frac{1}{3}\frac{2^6}{\pi^4} \tag{S6}$$

The dark photon generated current is set by the density of dark matter in the galaxy $\rho_{\text{DM}} = 0.4\,\text{GeV/cm}^3 = 2\pi \times 9.67 \times 10^{19}\,\text{GHz/cm}^3$:

$$J_{\text{DM}}^2 = 2\epsilon^2 m^4 A'^2 = 2\epsilon^2 m^2 \rho_{\text{DM}} \tag{S7}$$

where ϵ is the kinetic mixing angle between the dark photon and the visible matter. Substituting Eq. S7 into Eq. S5 yields the signal rate of photons deposited in the cavity by a dark photon dark matter candidate:

$$\frac{dN_{\rm HP}}{dt} = (n+1)\epsilon^2 \rho_{\rm DM} m_{\rm DM} G V \tau \tag{S8}$$

The total number of photons we expect to be deposited is determined by the photon rate and the integration time ($N_{\rm trials}\,\tau$) for each Fock state:

$$\begin{aligned} N_{\rm HP} &= \frac{dN_{\rm HP}}{dt} \times \tau \times N_{\rm trials} \\ &= (n+1)\epsilon^2 \rho_{\rm DM} m_{\rm DM} G V \tau^2 N_{\rm trials} \end{aligned} \tag{S9}$$

Comparing the first term in Eq. 4, we can rewrite the terms to obtain $\epsilon^2 = \frac{a_0}{\rho_{\rm DM} m_{\rm DM} G V}$.

A. *Calculating 90% confidence limit*

Expt. Parameter	Θ	σ_Θ
a_m	$1.9 \times 10^3 (\mathrm{s}^{-2})$	$\sigma_a = 9.807 \times 10^5 (\mathrm{s}^{-2})$
ω_s	5.965 GHz	$\sigma_{\omega_s} = 25$ Hz
Q_s	5.11×10^7	$\sigma_{Q_s} = 1.4 \times 10^5$
V	43.13 cm^3	$\sigma_V = 1.2$ cm^3
G	0.002	$\sigma_G = 0.0002$

TABLE S4. **Stimulated emission experimental parameters.** Systematic uncertainties of physical parameters in the experiment must be incorporated in determining the excluded dark photon mixing angle ϵ. The uncertainty in the dark photon (HP) conversion is determined in the previous section. The storage cavity frequency uncertainty is obtained by Ramsey interferometry. The quality factor of the cavity is given by $Q_s = \omega_s T_1^s$ so the uncertainty is calculated as $\sigma_{Q_s}^2 = (\omega_s \sigma_{T_1^s})^2 + (T_1^s \sigma_{\omega_s})^2$. The volume uncertainty is estimated by assuming machining tolerances of 0.005 inches in each dimension. The form a factor uncertainty is estimated from assuming 1% error in the simulated structure. Of the experimental quantities, the DP conversion has the largest systematic uncertainty.

By estimating the strength of the coherent drive in the absence of an external drive and the measured background counts for different Fock states, we perform a dark photon search. We determine the dark photon mixing angle ϵ that can be excluded at the 90% confidence level by using standard error propagation formula. We determine the standard deviation on ϵ given, we have the error estimates for all the parameters tabulated above.

We perform an ordinary least square (OLS) fit to the measured counts, and extract the fit parameters with their uncertainties tabulated in Table S5. The values of fit parameters obtained from performing a Maximum Likelihood Estimate (MLE) were comparable. The large statistical uncertainties on a_0 are due to the fact that the other two terms dominate the measured counts and fluctuations causing a_0 to swing up and down by a large amount.

Fitted Parameter	Θ	σ_Θ
$a_0\,(\mathrm{s}^{-2})$	1.9×10^3	7.662×10^5
$b\,(\mathrm{s}^{-1})$	-7.26	4.2×10^1
c_0	3.402×10^{-4}	4.292×10^{-4}
c_1	1.419×10^{-3}	4.0×10^{-4}
c_2	5.860×10^{-4}	4.222×10^{-4}
c_4	7.330×10^{-3}	6.732×10^{-4}

TABLE S5. **Fitted parameters.** Best fit and statistical uncertainties corresponding to each source of background counts. The Fock state with higher background counts have larger c value indicating that the source of counts is related to the state preparation step and thus, it is valid to perform a background subtraction to demonstrate the enhancement technique. For $\tau = 20\,\mu$s and $N_{\rm trials} \sim 20,000$, all three terms in Eq. (4) contribute roughly equally to the counts observed in Fig. 4.

The estimated value of $\epsilon_0 = 1.6 \times 10^{-15} \pm 3.30 \times 10^{-13}$, dominated by the error on a_0. We can now set the 90% confidence limit on the kinetic mixing angle term as $\epsilon^{90\%} = \epsilon_0 + 1.28\sigma_\epsilon = 4.24 \times 10^{-13}$. This leads us to exclude, with 90% confidence, dark photon with mixing angle $\epsilon^{90\%}$ greater than 4.24×10^{-13} as shown in Fig. S13.

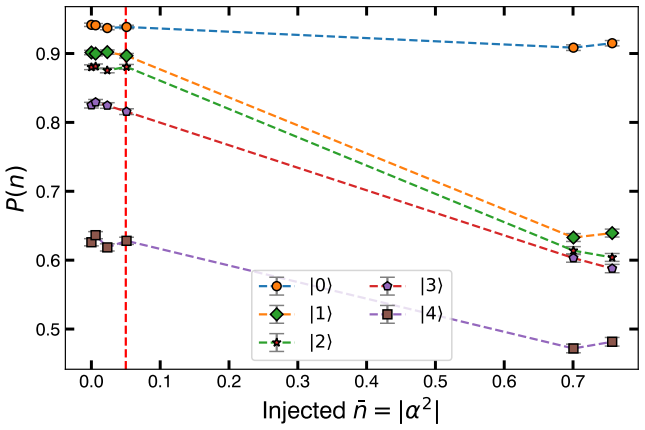

FIG. S12. **Fock state preparation with non-zero occupation in the cavity.** Measuring the Fock state preparation probability as a function of initializing the cavity with varying occupation before the OCT pulses. Red dashed line corresponds to the maximum tolerable injected number of photons where the fidelity changes significantly.

K. Dark photon parameter space exclusion

A dark photon candidate that could result in more detector counts than background counts is constrained by the cavity occupation number which degrades the fidelity of Fock state preparation in the cavity by a signif-

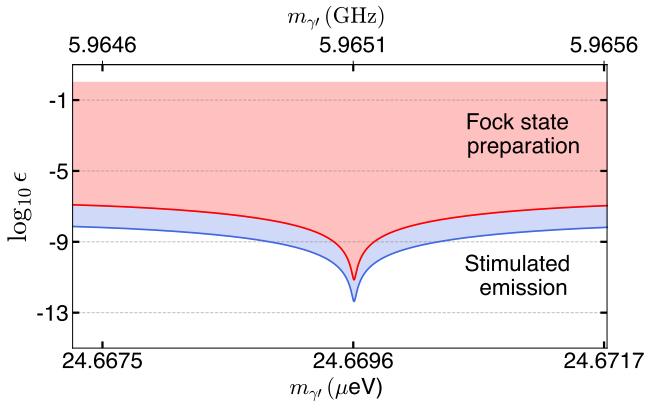

FIG. S13. **Excluded ϵ with $m_{\gamma\prime}$.** Shaded regions in the dark photon parameter space of coupling (ϵ) and mass (m_γ) are excluded with 90% confidence. The horizontal extent is set by the bandwidth of the number resolved qubit π-pulse which is insensitive to any drive outside the band. The vertical limit is set by the minimum ϵ which would result in dark photon rate greater than the value which would degrade the fidelity of Fock state preparation significantly.

icant amount. In order to estimate the same, the cavity is prepared with varied number of mean photons before applying the the OCT pulse. The resultant state is measured with the same procedure as the stimulated emission protocol to compute the fidelity. We observe that the fidelity changes significantly when the mean injected photon number goes above $\bar{n} > 0.05$ shown by the red dashed line in Fig. S12. The maximum number of photons sourced from the dark photon which is tolerable before the state preparation is out of control. In principle, we can exclude any value of ϵ which is above the red curve as it will break the first step of the stimulated emission experiment.

The above calculations assume an infinitely narrow dark matter line. To obtain the excluded region of the dark photon kinetic mixing angle, we must account for the lineshape of the dark matter [27]. We convolve the dark matter lineshape, characterized by $Q_{\mathrm{DM}} \sim 10^6$, to obtain the region shown in Fig. S13.

L. Outlook

The storage cavity contain an infinite set of discrete resonances each with a unique coupling to the dark matter. We focus only on the lowest order cavity mode that has a non-zero coupling to the dark matter as well as the qubit. In principle, the interactions between any modes and the dark matter could result in additional sensitivity to the dark photon. This would require the mode of interest to have a sufficiently large geometric form factor as well as a resolvable photon number dependent qubit shift. Future dark matter searches could employ structures with multiple resonances to enable multiple simultaneous searches [13].

Further advancements could be achieved by utilizing a system with a higher Q value and reduced demolition probability. By combining weakly coupled qubits with the Echoed Conditional Displacement (ECD) technique [18], Fock states can be prepared with high fidelity while also keeping the demolition probability low. Additionally, a detector with reduced errors from factors such as thermal population and readout fidelity would also improve the results.

References

[1] F. A. M. de Oliveira et al. "Properties of displaced number states". In: *Physical Review A* 41.5 (Mar. 1990), pp. 2645–2652. URL: https://doi.org/10.1103%2Fphysreva.41.2645.

[2] J.R. Johansson, P.D. Nation, and Franco Nori. "QuTiP: An open-source Python framework for the dynamics of open quantum systems". In: *Computer Physics Communications* 183.8 (Aug. 2012), pp. 1760–1772. URL: https://doi.org/10.1016/j.cpc.2012.02.021.

[3] J.R. Johansson, P.D. Nation, and Franco Nori. "QuTiP 2: A Python framework for the dynamics of open quantum systems". In: *Computer Physics Communications* 184.4 (Apr. 2013), pp. 1234–1240. URL: https://doi.org/10.1016/j.cpc.2012.11.019.

[4] A. B. Pippard and William Lawrence Bragg. "The surface impedance of superconductors and normal metals at high frequencies II. The anomalous skin effect in normal metals". In: *Proceedings of the Royal Society of London. Series A. Mathematical and Physical Sciences* 191.1026 (1947), pp. 385–399. URL: https://royalsocietypublishing.org/doi/abs/10.1098/rspa.1947.0122.

[5] G. E. H. Reuter, E. H. Sondheimer, and Alan Herries Wilson. "The theory of the anomalous skin effect in metals". In: *Proceedings of the Royal Society of London. Series A. Mathematical and Physical Sciences* 195.1042 (1948), pp. 336–364. URL: https://royalsocietypublishing.org/doi/abs/10.1098/rspa.1948.0123.

[6] Carlton M. Caves. "Quantum limits on noise in linear amplifiers". In: *Physical Review D* 26.8 (Oct. 1982), pp. 1817–1839. URL: https://doi.org/10.1103/physrevd.26.1817.

[7] T. Yamamoto et al. "Flux-driven Josephson parametric amplifier". In: *Applied Physics Letters* 93.4 (July 2008), p. 042510. URL: https://doi.org/10.1063/1.2964182.

[8] Christopher Eichler and Andreas Wallraff. "Controlling the dynamic range of a Josephson parametric amplifier". In: *EPJ Quantum Technology* 1.1 (Jan. 2014), p. 2. ISSN: 2196-0763. URL: https://doi.org/10.1140/epjqt2.

[9] Tanay Roy et al. "Broadband parametric amplification with impedance engineering: Beyond the gain-bandwidth product". In: *Applied Physics Letters* 107.26 (2015), p. 262601. URL: https://doi.org/10.1063/1.4939148.

[10] Esposito, Martina et al. "Development and characterization of a flux-pumped lumped element Josephson parametric amplifier". In: *EPJ Web Conf.* 198 (2019), p. 00008. URL: https://doi.org/10.1051/epjconf/201919800008.

[11] Akash V. Dixit et al. "Searching for Dark Matter with a Superconducting Qubit". In: *Phys. Rev. Lett.* 126 (14 Apr. 2021), p. 141302. URL: https://link.aps.org/doi/10.1103/PhysRevLett.126.141302.

[12] Srivatsan Chakram et al. "Multimode photon blockade". In: *Nature Physics* (June 2022). URL: https://doi.org/10.1038/s41567-022-01630-y.

[13] Srivatsan Chakram et al. "Seamless High-Q Microwave Cavities for Multimode Circuit Quantum Electrodynamics". In: *Physical Review Letters* 127.10 (Aug. 2021). URL: https://doi.org/10.1103/physrevlett.127.107701.

[14] H. Wang et al. "Measurement of the Decay of Fock States in a Superconducting Quantum Circuit". In: *Phys. Rev. Lett.* 101 (24 Dec. 2008), p. 240401. URL: https://link.aps.org/doi/10.1103/PhysRevLett.101.240401.

[15] Reinier W. Heeres et al. "Cavity State Manipulation Using Photon-Number Selective Phase Gates". In: *Phys. Rev. Lett.* 115 (13 Sept. 2015), p. 137002. URL: https://link.aps.org/doi/10.1103/PhysRevLett.115.137002.

[16] Nelson Leung et al. "Speedup for quantum optimal control from automatic differentiation based on graphics processing units". In: *Phys. Rev. A* 95 (4 Apr. 2017), p. 042318. URL: https://link.aps.org/doi/10.1103/PhysRevA.95.042318.

[17] Reinier W. Heeres et al. "Implementing a universal gate set on a logical qubit encoded in an oscillator". In: *Nature Communications* 8.1 (July 2017). URL: https://doi.org/10.1038/s41467-017-00045-1.

[18] Alec Eickbusch et al. "Fast universal control of an oscillator with weak dispersive coupling to a qubit". In: *Nature Physics* 18.12 (Oct. 2022), pp. 1464–1469. URL: https://doi.org/10.1038/s41567-022-01776-9.

[19] Navin Khaneja et al. "Optimal control of coupled spin dynamics: design of NMR pulse sequences by gradient ascent algorithms". In: *Journal of Magnetic Resonance* 172.2 (Feb. 2005), pp. 296–305. URL: https://doi.org/10.1016%2Fj.jmr.2004.11.004.

[20] K. E. Cahill and R. J. Glauber. "Density Operators and Quasiprobability Distributions". In: *Physical Review* 177.5 (Jan. 1969), pp. 1882–1902. URL: https://doi.org/10.1103/physrev.177.1882.

[21] Yvonne Y. Gao. "Multi-Cavity Operations in Circuit Quantum Electrodynamics". PhD thesis. Boulder: Yale University, 2018. URL: https://rsl.yale.edu/sites/default/files/files/RSL_Theses/Yvonne%20Gao_thesis_2018.pdf.

[22] Huaixiu Zheng et al. *Accelerating dark-matter axion searches with quantum measurement technology*. 2016. URL: https://arxiv.org/abs/1607.02529.

[23] L. Sun et al. "Tracking photon jumps with repeated quantum non-demolition parity measurements". In: *Nature* 511.7510 (July 2014), pp. 444–448. URL: https://doi.org/10.1038%2Fnature13436.

[24] Connor T. Hann et al. "Robust readout of bosonic qubits in the dispersive coupling regime". In: *Physical Review A* 98.2 (Aug. 2018). URL: https://doi.org/10.1103/physreva.98.022305.

[25] X. Y. Jin et al. "Thermal and Residual Excited-State Population in a 3D Transmon Qubit". In: *Physical Review Letters* 114.24 (June 2015). URL: https://doi.org/10.1103/physrevlett.114.240501.

[26] Ning Lu. "Effects of dissipation on photon statistics and the lifetime of a pure number state". In: *Physical Review A* 40.3 (Aug. 1989), pp. 1707–1708. URL: https://doi.org/10.1103%2Fphysreva.40.1707.

[27] Joshua W. Foster, Nicholas L. Rodd, and Benjamin R. Safdi. "Revealing the dark matter halo with axion direct detection". In: *Physical Review D* 97.12 (June 2018). URL: https://doi.org/10.1103/physrevd.97.123006.